Nanoscale

PAPER

Check for updates

The role of composition and diameter in the crystal purity of InAs$_x$P$_{1-x}$ nanowires

Giada Bucci, [ID] [a] Vladimir G. Dubrovskii, [ID] [b] Valentina Zannier, [ID] *[a] Fabio Beltram [ID] [a] and Lucia Sorba [ID] [a]

Ternary InAs$_x$P$_{1-x}$ nanowires are widely considered promising building blocks for fundamental studies and applications in nano- and opto-electronics. However, it is admittedly challenging to maintain the necessary control over the crystal purity of nanowires. Furthermore, the crystal phase trends in ternary III–V nanowires remain generally unknown. In this work, we present wurtzite InAs$_x$P$_{1-x}$ nanowires with different compositions x, ranging from 0 to 0.54, grown *via* chemical beam epitaxy on InP(111)B substrates using Au colloidal catalysts of different diameters. Transmission electron microscopy studies reveal that a pure wurtzite phase of the nanowires requires larger InAs fractions x for larger diameters of Au colloids (in particular, $x = 0.36$ for 20 nm diameter and $x = 0.54$ for 30 nm diameter Au colloids). We developed a model for the critical composition of thin vapor–liquid–solid III–V ternary nanowires x_c corresponding to the transition from a polytypic structure at $x < x_c$ to a pure wurtzite structure at $x > x_c$. For the InAs$_x$P$_{1-x}$ material, the critical composition increases with the nanowire diameter, which explains our experimental findings. These results shed more light on the composition- and diameter-dependent polytypism, offering valuable insights for the design and crystal phase control of InAs$_x$P$_{1-x}$ and other III–V ternary nanowires.

1. Introduction

III–V semiconductor nanowires (NWs) have been extensively studied due to their unique structural, electronic, and optical properties. Thanks to their high aspect ratio, NWs can relax strain radially, enabling the integration of highly lattice-mismatched materials without introducing dislocations. This feature enables greater flexibility in realizing NW heterostructures composed of dissimilar materials and bandgap engineering in such heterostructures compared to *epi*-layers.[1] NWs are often synthesized *via* a metal-assisted vapor–liquid–solid (VLS) growth method. By tuning the growth conditions, substrate orientation, catalyst material and NW diameter, both hexagonal wurtzite (WZ) and cubic zincblende (ZB) crystal phases can be obtained in III–V NWs.[2] A pure WZ phase is never observed in bulk III–V materials, but it is easily achieved in binary III–V NWs. This crystal phase is of great interest due to several intriguing properties, like the possibility of realizing the vanishing fine-structure splitting in WZ quantum dots (QDs)[3] or obtaining a direct band gap structure of GaP, AlGaAs

and some other III–V materials.[4,5] Recently, significant efforts have been devoted to the synthesis and investigation of III–V ternary NWs, which offer promising applications due to their bandgap tunability and the emergence of novel properties. Among ternary alloys, InAs$_x$P$_{1-x}$ has attracted particular interest due to its potential in a wide range of technologies. This material exhibits excellent piezoelectric properties[6,7] and a tunable direct band gap ranging from 0.351 eV to 1.351 eV,[8] making it highly suitable for applications in optoelectronics, quantum computing, and quantum information technologies. Additionally, the low effective mass and high electron mobility in InAs$_x$P$_{1-x}$ are attractive for the realization of high-performance electronic devices. Significant research efforts have focused on the synthesis of InAs$_x$P$_{1-x}$ quantum dots in InP NWs, which are promising for single photon emission.[9,10]

Notably, improved optical properties have been observed when these QDs are inserted into an InAs$_x$P$_{1-x}$ segment with a reduced InAs fraction,[11] a strategy that requires precise control over the formation of ternary NWs. To date, ternary alloy engineering in NWs has mainly concentrated on compositional control.[8,12,13] However, a defect-free structure of InAs$_x$P$_{1-x}$ is absolutely required for all envisioned applications, because structural defects are known to degrade both the electronic and optical performance of the material. Due to the different band structures of the WZ and ZB phases, their intermixing in the same NW introduces electron and phonon

[a]NEST, Scuola Normale Superiore of Pisa and Istituto Nanoscienze - Consiglio Nazionale delle Ricerche (CNR), 56127 Pisa, Italy.
E-mail: valentina.zannier@nano.cnr.it
[b]Faculty of Physics, St. Petersburg State University, Universitetskaya Embankment 7-9, 199034 St. Petersburg, Russia

scattering at the interfaces and the formation of charge traps.[14–16] Avoiding polytypism remains challenging even in binary InP and InAs NWs, since the NW growth along the ⟨111⟩ direction promotes the formation of stacking faults due to the small energy difference between the WZ and ZB stacking in this direction.[17] The crystal phase purity in both InP and InAs NWs has been shown to depend on several growth parameters, including growth temperature, V/III ratio, total precursor fluxes and diameter. The latter dependence has been ascribed to the Gibbs–Thomson effect.[18] Defect-free WZ InP NWs have been demonstrated, to the best of our knowledge, only in NWs with very small diameters (up to 20 nm).[16] In contrast, InAs NWs tend to form in the WZ crystal phase even at larger diameters, although the diameter dependence has also been reported for this material.[18] Here, we present a study on the crystal phase purity of ternary $InAs_xP_{1-x}$ NWs as a function of the NW diameter and chemical composition. We find the existence of a critical composition, above which the $InAs_xP_{1-x}$ NWs are pure WZ. This critical composition increases with the NW diameter.

In general, the crystal phase trends in VLS III–V ternary NWs have not been systematically quantified and remain largely unknown. Consequently, we have developed a semi-quantitative model for the composition- and diameter-dependent polytypism in such NWs and show that the percentage of the WZ phase is generally a function of two variables, the NW diameter $2R$ and composition, represented by the InAs fraction in the ternary alloy, x. The diameter dependence originates from the contributions of edges separating the NW facets to the overall surface energy balance, which become important for thin NWs. Hence, the critical composition x_c in VLS III–V ternary NWs, corresponding to the transition from a polytypic WZ/ZB intermix at $x < x_c$ to a pure WZ structure at $x > x_c$, depends on the NW diameter. For the $InAs_xP_{1-x}$ material, the critical composition increases with the NW diameter, which explains the data. This work extends the approaches originally developed for binary systems to a more complex case of VLS III–V ternary NWs, providing insights into the interplay between the diameter, composition and crystal phase. To the best of our knowledge, we demonstrate for the first time a diameter-dependent critical composition required to achieve phase-pure ternary wurtzite NWs. The results should be useful from a general perspective and for crystal phase engineering in thin $InAs_xP_{1-x}$ NWs, and can be translated to other material systems.

2. Results and discussion

Defect-free WZ InP NWs grown from 10 nm diameter Au colloids have already been reported in the literature.[19] At this diameter, the WZ crystal phase is energetically preferred also for InAs NWs.[18] To explore the dependence of the crystal phase on the NW diameter and composition, we decided to focus on larger diameters, where a mixed ZB/WZ crystal phase typically occurs in both binary NWs.[18,20,21] Different samples were

grown using Au colloidal nanoparticles (NPs) of 20 nm and 30 nm diameters, which resulted in the NW diameters of ~25 nm and up to ~45 nm, respectively. All the NW samples investigated in this work were grown using the same procedure. After heating the InP (111)B substrate to 400 ± 10 °C under a *tert*-butyl phosphine (TBP) line pressure of 1 Torr, the NW growth was initiated by introducing trimethylindium (TMIn), TBP and, when required, *tert*-butyl arsine (TBAs). The growth was carried out for 120 minutes to obtain NWs with lengths of 1090 ± 200 nm for 20 nm diameter colloids and 330 ± 30 nm for 30 nm diameter colloids.

Fig. 1 shows the results for the NWs grown from 20 nm diameter NPs. Additional TEM images are reported in section S1 of the SI. In panel (a), a 45°-tilted view SEM image shows an ensemble of binary InP NWs grown using TMIn and TBP precursor line pressures of 0.30 Torr and 1.05 Torr, respectively. Two different NW morphologies are highlighted with orange and green boxes. The former, referred to as "type 1" in the following, is characterized by the enhanced radial growth, indicated by the red arrow in Fig. 1(a). This enhancement has pre-
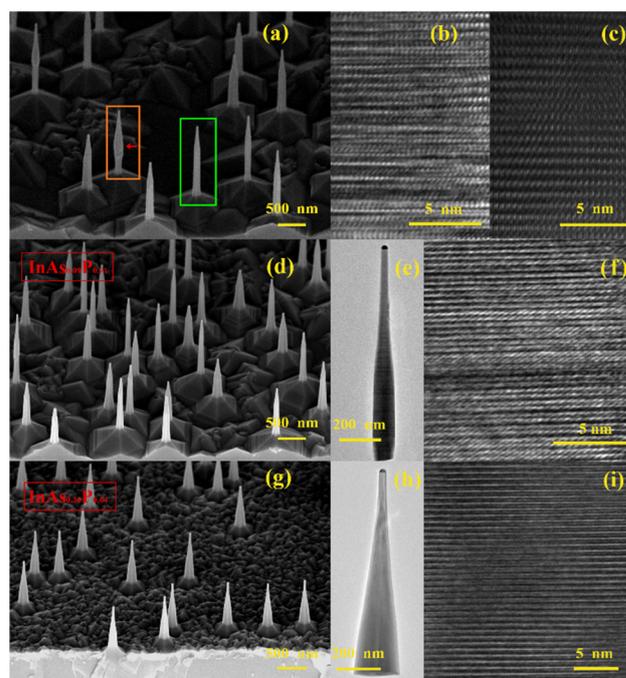

Fig. 1 (a) 45°-tilted SEM image of InP NWs grown from 20 nm Au NPs. Orange and green boxes highlight the NWs of type 1 (tapered morphology and high stacking fault density) and type 2 (untapered morphology and nearly pure WZ phase), respectively. (b) Representative HRTEM image of type 1 NWs, showing the presence of high density crystal defects; (c) representative HRTEM image of type 2 NWs, showing good crystal quality in the WZ phase for this morphology; (d) 45°-tilted SEM image of the $InAs_{0.09}P_{0.91}$ NW ensemble, with its TEM image in panel (e) and HRTEM image in panel (f), showing the presence of stacking faults also in this sample; (g) 45°-tilted SEM image of the $InAs_{0.36}P_{0.64}$ NW ensemble, with its TEM image in panel (h) and HRTEM image in panel (i), showing the defect-free WZ crystal phase of excellent quality.

viously been reported in the literature[22] and is attributed to the NW sections with a high density of stacking faults. This is also confirmed in our sample. Panel (b) of Fig. 1 presents a high-resolution transmission electron microscopy (HRTEM) image of such a NW, showing the presence of crystal defects. In contrast, the latter type of NW, labelled "type 2" in the following, displays a nearly untapered morphology with no significant radial growth or bulges along its length. This morphology is characterized by a low stacking fault density or even a fully defect-free WZ crystal phase, as demonstrated by the HRTEM image in Fig. 1(c).

To identify the optimal growth conditions for obtaining pure WZ binary InP NWs with an untapered geometry, we studied the growth under different V/III ratios by varying the TBP line pressure from 0.50 Torr to 1.50 Torr and keeping the TMIn pressure constant at 0.30 Torr. In all cases, we obtained NW ensembles with both morphologies. Hence, we selected the growth conditions that minimized the occurrence of type 1 NWs with high stacking fault density. Based on this criterion, the optimal TBP line pressure was identified as 1.05 Torr (*i.e.*, the sample in Fig. 1(a)). Under these precursor fluxes, approximately 42% of the NWs exhibit the unwanted type 1 morphology, while the remaining portion corresponds to type 2 morphology. A total of 50 NWs were analyzed for the percentage estimation. After selecting the best conditions for binary InP NWs of this diameter, we investigated the growth of $InAs_xP_{1-x}$ ternary NWs. To evaluate the effect of As incorporation on the crystal purity of the NWs, we grew a series of samples at the same temperature of 400 °C, keeping the TMIn line pressure at 0.30 Torr and the constant total group-V line pressure (TBAs + TBP) at 1.05 Torr. Fig. 1(d) and (g) show the SEM images of two different $InAs_xP_{1-x}$ samples, grown using TBAs and TBP line pressures of 0.10 Torr and 0.95 Torr, respectively (resulting in $x = 0.09$), and 0.20 Torr and 0.85 Torr, respectively (resulting in $x = 0.36$). TEM analysis of the first sample in Fig. 1(e) and (f) reveals that stacking faults are still present in the $InAs_{0.09}P_{0.91}$ NWs, but their occurrence is reduced compared to InP NWs. Only ~36% of $InAs_{0.09}P_{0.91}$ NWs exhibit crystal defects. In contrast, Fig. 1(h) shows a TEM image of a defect-free $InAs_{0.36}P_{0.64}$ WZ NW. The corresponding HRTEM image in panel (i) demonstrates the absence of any stacking faults. All NWs of this sample exhibit the defect-free WZ crystal phase. Therefore, a higher fraction of InAs "x" in ternary $InAs_xP_{1-x}$ NWs grown from 20 nm Au NPs improves the crystal quality in the WZ phase. By comparing the SEM images of these samples, it is evident that the incorporation of As into the NWs leads to increased radial growth, resulting in more-tapered NWs grown at the same temperature. This effect is likely due to the higher sticking coefficient of As than that of P,[8] which enhances the nucleation probability on the NW sidewalls. Additionally, the average axial growth rate decreases monotonically with the increase of the As fraction from 13 nm min^{-1} in pure InP NWs to 9 nm min^{-1} in $InAs_{0.36}P_{0.64}$ NWs.

Fig. 2 presents the results of a similar study for NWs grown from Au NPs of 30 nm diameter. Additional TEM images are shown in section S2 of the SI. Panel (a) shows a 45°-tilted SEM
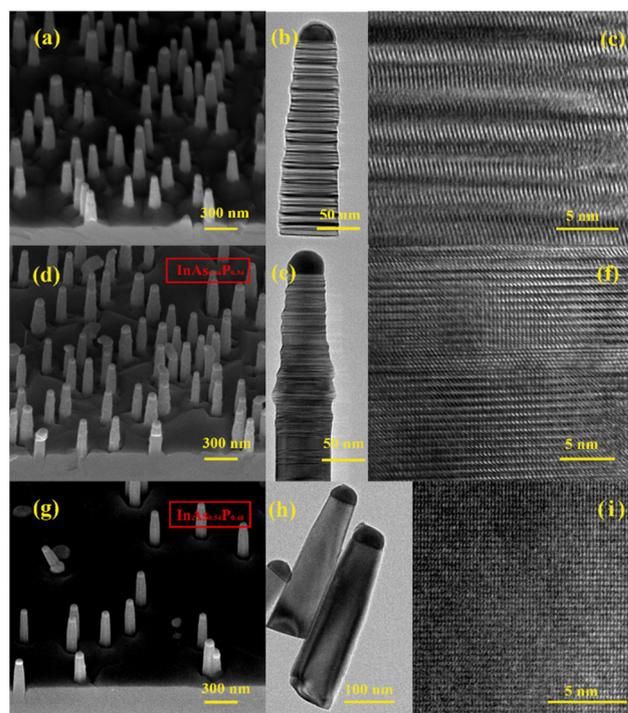

Fig. 2 (a) 45°-tilted SEM image of InP NWs grown from 30 nm Au NPs, with the corresponding TEM image in panel (b) and HRTEM image in panel (c), respectively; (d) 45°-tilted SEM image of $InAs_{0.46}P_{0.54}$ NWs, with the corresponding TEM image in panel (e) and HRTEM images in panel (f), respectively; (g) 45°-tilted SEM image of $InAs_{0.54}P_{0.46}$ NWs that exhibit a pure WZ crystal phase, as demonstrated by the TEM image in panel (h) and the HRTEM image in panel (i).

image of an ensemble of binary InP NWs grown at the TMIn and TBP line pressures of 0.30 Torr and 0.40 Torr, respectively. As above, several V/III ratios were explored to identify the optimal growth conditions for binary InP NWs. However, in this case, the two distinct morphologies observed for 20 nm diameter colloids are not evident. The NWs appear highly defective across the entire range of TBP line pressures. Employing a TBP line pressure of 1.05 Torr, as for thinner NWs in Fig. 1(a), resulted in NWs with a high radial growth rate and limited elongation. Consequently, we decided to lower the TBP flux to 0.40 Torr, which gave nearly untapered NWs with negligible radial growth, as demonstrated in Fig. 2(a). Fig. 2(b) and (c) show the TEM and HRTEM images of a representative NW from this sample, where a high stacking fault density is clearly visible. The transition from a mixed ZB/WZ structure to a pure WZ phase is observed for higher InAs fractions in NWs, as observed earlier for 20 nm Au NPs. However, achieving a pure WZ phase requires a higher InAs fraction than that for 20 nm Au NPs. Fig. 2(d) shows an ensemble of $InAs_{0.46}P_{0.54}$ NWs grown under TBAs and TBP line pressures of 0.15 Torr and 0.25 Torr, respectively. These NWs remain highly defective, as demonstrated by the representative TEM image in Fig. 2(e) and the corresponding HRTEM image in Fig. 2(f). Defect-free WZ NWs shown in Fig. 2(g), (h) and (i)

are grown under TBAs and TBP line pressures of 0.20 Torr and 0.20 Torr, respectively. This results in a higher InAs fraction of $x = 0.54$, and does not lead to any significant change in either the axial or radial growth rate. In contrast to the earlier suggestion,[22] lower axial growth rates are not the only requirement for achieving a pure WZ phase in III–V NWs, at least in our case of ternary InAs$_x$P$_{1-x}$ NWs. It should be noted, however, that the increased InAs fraction results in a lower vertical yield of NWs, with a significant fraction of the NWs failing to nucleate. This can be seen in Fig. 2(g), where some catalyst NPs without any NWs are clearly visible on the substrate. This should be related to difficult nucleation of NWs on the substrate surface under the growth conditions that were chosen to obtain untapered NWs in the pure WZ phase rather than to maximize their yield.

It is clear at this point that the crystal phase of ternary InAs$_x$P$_{1-x}$ NWs strongly depends on the InAs fraction, with a critical composition x_c at which the structure transforms from highly defective to pure WZ. This critical composition increases with the NW diameter (or, equivalently, with the Au NP diameter from which the NWs grow). Previous studies have speculated that defect formation in both InP and InAs binary NWs is related to the concentration of liquid In in the catalyst droplets.[18,19] Therefore, we performed TEM-EDS measurements of the droplet compositions and contact angles for all the NWs discussed above. At least 20 NWs were investigated for each sample. These post-growth measurements were taken after cooling the samples in the absence of group V fluxes. This method has previously been demonstrated not to significantly alter the catalyst composition in binary NWs, providing an estimation of the catalyst composition during growth.[23] Here, we used the same cooling procedure, so that we can compare the measured composition of the catalyst nanoparticles of the different samples after growth. The data in Table 1 show that the In/Au ratio inside the catalysts varies between 20 and 30 nm diameter samples. However, there is no significant change in the NP composition between binary InP and ternary InAs$_x$P$_{1-x}$ NWs. These results indicate that, unlike in the case of binary InP NWs,[19] the crystal phase purity of ternary InAs$_x$P$_{1-x}$ NWs is not directly linked to the In content in the catalyst NPs (of course, both As and P atoms were not detected in the NPs due to their high volatility). Additionally, Table 1 shows no significant change in the average contact angle of the NPs on top of different NWs.

Table 1 In and Au percentages and contact angles of the NPs on top of different InAs$_x$P$_{1-x}$ NWs

NP diameter (nm)	InAs fraction x	In (at%)	Au (at%)	Average contact angle (°)
20	0	54 ± 2	46 ± 2	94 ± 5
20	0.09	52 ± 8	48 ± 8	87 ± 5
20	0.36	49 ± 3	51 ± 3	93 ± 3
30	0	65 ± 2	35 ± 2	84 ± 8
30	0.46	68.6 ± 0.9	31.4 ± 0.9	100 ± 5
30	0.54	65.3 ± 0.8	34.7 ± 0.8	98 ± 3

3. Modeling

To understand the composition- and diameter-dependent polytypism and crystal phase purity of ternary InAs$_x$P$_{1-x}$ NWs under optimal conditions, we have developed the following energetic model. In the first approximation, we ignored the vapor–solid growth of tapered shells around the NW cores, thus assuming that the crystal phase is determined during the VLS growth step of the NW core. This was earlier justified for binary III–V NWs, where the tapered shells inherit the crystal phase of the VLS cores.[24–27] According to ref. 26–31, the conditions for the formation of VLS NWs in the WZ phase are equivalent to the preferred formation of vertical WZ facets relative to the truncated ZB facets:

$$\Delta\gamma = \frac{\gamma_\varphi}{\cos\varphi} - \gamma_p \tan\varphi - \gamma_S + \gamma_L \sin\beta > 0. \quad (1)$$

Here, β is the droplet contact angle, φ is the angle of the truncated facet with respect to the vertical facet, γ_φ is the solid–liquid surface energy of the truncated facet, γ_P is the solid–liquid surface energy of the horizontal facet under the droplet, γ_S is the solid–vapor surface energy of the vertical WZ facet, and γ_L is the liquid–vapor surface energy of the droplet. The two solid–liquid surface energies γ_φ and γ_P are phase-independent.[24,32] The geometries of the NW tip and the interfaces of interest are illustrated in Fig. 3(a). The surface energies
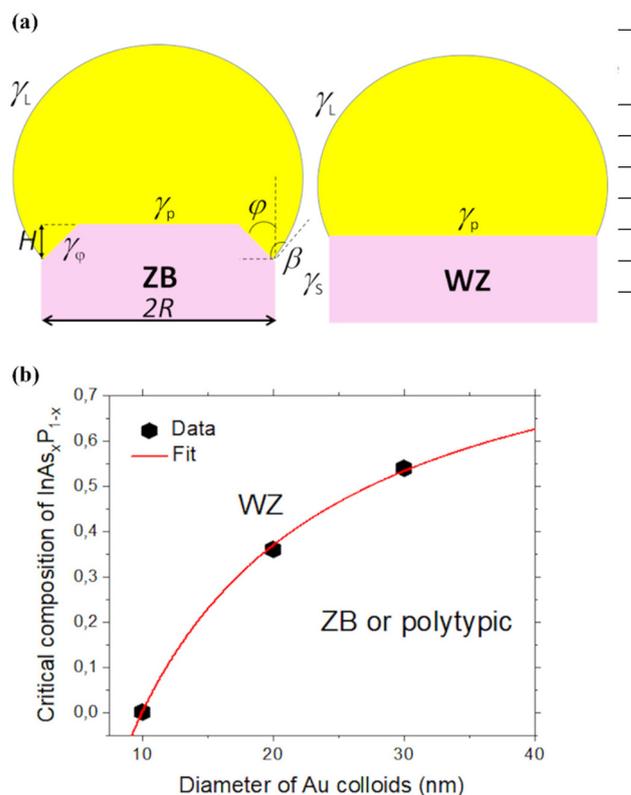

Fig. 3 (a) Illustration of the truncated ZB and planar WZ growth interfaces under the catalyst droplets, showing the surface energies of interest. (b) Critical composition of InAs$_x$P$_{1-x}$ NWs x_c *versus* the Au nanoparticle diameter (symbols), fitted with eqn (6) at $x_c^\infty = 0.96$, $A = 5$ nm and $B = 3$ nm (line).

γ in eqn (1) are usually considered radius-independent.[26–32] This is valid for thick enough NWs with negligible contribution of the edges separating the side facets. For thin NWs, these edges start to play an important role in the total formation energy of hexahedral NWs.[24,33–35] The liquid surface and planar horizontal facet under the droplet have no edges; hence, γ_L and γ_P are independent of the NW top radius (which is directly related to the nominal radius of Au colloids R).

Six equivalent facets of truncated ZB NWs and vertical WZ NWs are separated by edges. The surface energies γ per the surface area are $\sim RH$, where H is the truncation height (see Fig. 3(a)). Hence, the edge energies are inversely proportional to R. The total surface energies with the edge contributions are given by ref. 24 and 34:

$$\gamma_\varphi = \Gamma_\varphi + \frac{\varepsilon_\varphi}{R}, \quad \gamma_S = \Gamma_S + \frac{\varepsilon_S}{R}. \tag{2}$$

Here, Γ denotes the surface energy of flat facets and ε is the specific edge energy per unit length, with $\gamma_\varphi \to \Gamma_\varphi$ at large R. For InAs$_x$P$_{1-x}$ ternary NWs, the solid–vapor and liquid–vapor surfaces and edge energies depend on the composition x. The surface energies and edge energies of III–V ternary NWs in both ZB and WZ phases are unknown. Therefore, we used the simplest linear dependence on the composition in the first approximation:[1,13]

$$\Gamma_\varphi = \Gamma_\varphi^0\left(1 - c_\varphi^\Gamma x\right), \quad \varepsilon_\varphi = \varepsilon_\varphi^0\left(1 - c_\varphi^\varepsilon x\right),$$
$$\Gamma_S = \Gamma_S^0\left(1 - c_S^\Gamma x\right), \quad \varepsilon_S = \varepsilon_S^0\left(1 - c_S^\varepsilon x\right), \tag{3}$$
$$\gamma_p = \gamma_P^0\left(1 - c_p x\right).$$

Here, the surface and edge energies labelled "0" correspond to pure InP NWs, and x-independent coefficients c describe linear interpolation of the surface and edge energies between pure InP and InAs. According to the calculations of ref. 36, the vapor–solid surface energy Γ_S^0 of unpassivated vertical WZ facets $(1\bar{1}00)$ and $(11\bar{2}0)$ at zero temperature is 23.5% lower for InAs NWs, corresponding to positive $c_S^\Gamma = 0.235$. This corresponds to the well-known trend of a stable WZ phase in binary InAs NWs, where the ZB stacking is the exception rather than the rule.[12,13] However, nothing is known about the edge energies of ternary NWs and the solid–liquid surface energies Γ_φ and γ_p, which is why the other coefficients c in eqn (3) can be of either sign.

The surface energy of a liquid droplet should be independent of the negligibly small concentrations of P and As atoms, and even of the Au concentration, because the lower surface energy liquid In accumulates at the droplet surface.[28–30] The droplet contact angle β is the only kinetic parameter in eqn (1). It generally depends on the total V/III ratio and As/P flux ratio (and hence the composition x) due to kinetic growth effects.[23] We used linear interpolation of $\sin\beta$ in eqn (1) of the form: $\sin\beta(x) \cong \sin\beta_0 + (\cos\beta_0)c_\beta x$, with the coefficient c_β, and β_0 is the average contact angle of the droplets on top of pure InP NWs. This assumes a small variation of the contact angle compared to β_0. Post-growth measurements (see Table 1) show that the average contact angle of all the NWs is only slightly above 90°. In this case, the composition dependence of the contact angle is very weak, but this is not critical for our semi-quantitative model.

Using eqn (2) and (3) in eqn (1), we obtain the condition of the preferred WZ phase formation in the form $\Delta\gamma(R, x) > 0$. This allows us to determine the critical composition x_c corresponding to the ZB-to-WZ phase transition as a function of the radius R. After some manipulations, eqn (1) can be put in the form

$$\Delta\gamma_0 - \frac{a}{R} + \left(d + \frac{b}{R}\right)x > 0, \tag{4}$$

with

$$\Delta\gamma_0 = \frac{\Gamma_\varphi^0}{\cos\varphi} - \gamma_P^0\tan\varphi - \Gamma_S^0 + \gamma_L\sin\beta_0,$$
$$a = \varepsilon_S^0 - \frac{\varepsilon_\varphi^0}{\cos\varphi},$$
$$b = \varepsilon_S^0 c_S^\varepsilon - \frac{\varepsilon_\varphi^0 c_\varphi^\varepsilon}{\cos\varphi}, \tag{5}$$
$$d = \Gamma_S^0 c_S^\Gamma + \gamma_P^0 c_P\tan\varphi + \gamma_L(\cos\beta_0)c_\beta - \frac{\Gamma_\varphi^0 c_\varphi^\Gamma}{\cos\varphi}.$$

Clearly, $\Delta\gamma_0$ is the surface energy difference that determines the crystal phase of thick InP NWs at a contact angle β_0, a/R is the composition-independent edge contribution, and the x term contains two contributions from the surface (d) and edge (b/r) energies. The WZ phase is energetically preferred when

$$x > x_c = x_c^\infty\frac{R - A}{R + B}, \tag{6}$$

with

$$x_c^\infty = -\frac{\Delta\gamma_0}{d}, \quad A = \frac{a}{\Delta\gamma_0}, \quad B = \frac{b}{d}. \tag{7}$$

The parameters x_c^∞, A and B combine together the largely unknown energetic factors influencing the crystal phase trend in thin III–V ternary NWs, and yield a simple analytical shape of the critical curve $x_c(R)$. For x below the critical curve $x_c(R)$, the crystal phase can be polytypic rather than pure ZB due to a periodically changing geometry of the growth interface.[26,30]

Our model describes different crystal phase trends depending on the signs and magnitudes of the coefficients in eqn (6). The data shown in Fig. 3(b) demonstrate that the pure WZ phase of InAs$_x$P$_{1-x}$ grown in our experiments requires higher fractions of InAs for larger radii. The first data point in Fig. 3(b) corresponds to WZ InP NWs at $R = 5$ nm,[19] which requires $A = 5$ nm in eqn (6). A monotonically increasing dependence $x_c(R)$ in the investigated range of NW compositions and Au radii requires positive x_c^∞ and positive A. From eqn (7), this corresponds to differently signed coefficients $\Delta\gamma_0$ and d, and equally signed coefficients $\Delta\gamma_0$ and a ($\Delta\gamma_0 > 0$, $a > 0$ and $d < 0$, or $\Delta\gamma_0 < 0$, $a < 0$ and $d > 0$). The sign of B in eqn (6) is less important. For example, the data points can reasonably be fitted by $x_c = x_c^\infty(1 - A/R)$ at $B \cong 0$. The fit shown in Fig. 3(b) is obtained with $x_c^\infty = 0.96$, $A = 5$ nm and $B = 3$ nm. This corres-

ponds to the pure WZ phase of very thin InP NWs ($R \leq 5$ nm), ZB or the polytypic phase of thicker InP NWs, and the almost pure WZ phase of thick InAs NWs under our growth conditions. The trend of a more stable WZ phase of InAs NWs relative to InP and all other binary III–V NWs is well known and has been reproduced by different epitaxy techniques.[24,37]

Experimental details

The NW samples in this work are epitaxially grown by means of Au-assisted VLS growth in a Riber C-21 chemical beam epitaxy (CBE) system. Trimethylindium (TMIn), pre-cracked *tert*-butyl arsine (TBAs) and *tert*-butyl phosphine (TBP) are used as gaseous metal–organic precursors, for which it is possible to measure the line pressures as a reference for the fluxes introduced into the chamber. The substrate temperature is measured with a pyrometer, providing an accuracy of ±10 °C. Prior to the mounting of the substrate in the reactor chamber, Au catalyst nanoparticles are deposited through colloidal dispersion. Commercial aqueous solutions of Au colloids with nominal diameters of 20 nm and 30 nm (BBInternational EM. GCnn) are employed. Fe-doped InP(111)B substrates are first functionalized by wetting the surface through dropcasting of 0.1% poly-L-lysine solution for 30s, then rinsed in deionized water and blow-dried under N_2 flux. The colloid solution is dropcast onto the substrate surface, which is then rinsed in DI water and blow-dried. Before inserting the sample into the growth chamber, the substrate is outgassed at 300 °C on a heating stage for around five minutes to get rid of the moisture.

After growth, the samples are imaged employing scanning electron microscopy (Zeiss Merlin SEM) operating at 5 kV, from both top and side views, to check the NW morphology, and the ternary alloy composition of the NWs is measured through energy-dispersive X-ray spectroscopy (EDS) analysis employing a Bruker Quantax EDS system mounted on a Zeiss Ultraplus scanning electron microscope. Transmission electron microscopy (TEM), scanning transmission electron microscopy (STEM) and STEM–EDS of the catalyst nanoparticles were performed using a JEOL JEM-F200 multipurpose microscope, working at 200 kV and equipped with a Schottky field-emission gun and a silicon drift detector. TEM images were recorded with a GATAN RIO16 CMOS camera. The crystal structure of 20 NWs per sample is analyzed by TEM for statistical purposes. The percentage of defective NWs is calculated by counting the number of NWs in which stacking faults are observed, regardless of their density and distribution along the growth axis, over the total number of NWs measured.

4. Conclusions

In summary, we have demonstrated Au-catalyzed formation of $InAs_xP_{1-x}$ NWs in a pure WZ crystal phase for high enough fractions of InAs in the ternary alloy. The critical composition

x_c required for the formation of the pure WZ phase in ternary NWs increases from 0.36 for 20 nm diameter to 0.54 for 30 nm diameter Au nanoparticles, and is expected to increase further for larger diameters. While a more predominant WZ phase in binary InAs NWs relative to InP NWs has been known, the composition- and diameter-dependent crystal phase purity of Au-catalyzed VLS ternary $InAs_xP_{1-x}$ NWs with small diameters has been studied here for the first time to our knowledge. The developed model explains the data on surface energetic grounds, where the effective surface energies vary with the NW composition, and the diameter dependence is due to the edge contributions to the overall energy balance. A more advanced study should include kinetic contributions to the phase purity of III–V ternary NWs. These obtained results call for further systematic investigations of the crystal phase transitions in $InAs_xP_{1-x}$ NWs under a wider range of growth conditions and Au nanoparticle diameters, and similar investigations for other III–V ternary NWs grown by different methods.

Author contributions

G. B., V. Z. and L. S. performed the growth of the NWs; G. B. performed the TEM measurements; V. G. D. carried out the modeling part; F. B. contributed to writing, review and editing. All authors have read and agreed to the published version of the manuscript.

Conflicts of interest

There are no conflicts to declare.

Data availability

The authors confirm that all data supporting the findings of this study are available within the manuscript.

Supplementary information is available. In the SI, additional TEM images of the samples presented in the main text are provided. S1 contains the images of NWs obtained with 20 nm diameter colloids, S2 the the images of NWs obtained with 30 nm diameter colloids. See DOI: **https://doi.org/10.1039/d5nr02409a**

Acknowledgements

References

1 J. Johansson and K. A. Dick, *CrystEngComm*, 2011, **13**, 7175.

2 P. Caroff, J. Bolinsson and J. Johansson, *IEEE J. Sel. Top. Quantum Electron.*, 2011, **17**, 829–846.

3 R. Singh and G. Bester, *Phys. Rev. Lett.*, 2009, **103**, 063601.

4 B. C. da Silva, O. D. D. Couto, H. T. Obata, M. M. de Lima, F. D. Bonani, C. E. de Oliveira, G. M. Sipahi, F. Iikawa and M. A. Cotta, *Sci. Rep.*, 2020, **10**, 7904.

5 S. Assali, J. Greil, I. Zardo, A. Belabbes, M. W. A. De Moor, S. Koelling, P. M. Koenraad, F. Bechstedt, E. P. A. M. Bakkers and J. E. M. Haverkort, *J. Appl. Phys.*, 2016, **120**, 044304.

6 I. Kim, H. S. Kim and H. Ryu, *Molecules*, 2019, **24**, 3249.

7 J. Liu, H. Yang, V. Khayrudinov, H. Lipsanen, H. Nie, K. Yang, B. Zhang and J. He, *Photonics Res.*, 2021, **9**, 1811–1819.

8 A. I. Persson, M. T. Björk, S. Jeppesen, J. B. Wagner, L. R. Wallenberg and L. Samuelson, *Nano Lett.*, 2006, **6**, 403–407.

9 D. Dalacu, P. J. Poole and R. L. Williams, *Nanotechnology*, 2019, **30**, 232001.

10 G. Bucci, V. Zannier, F. Rossi, A. Musiał, J. Boniecki, G. Sęk and L. Sorba, *ACS Appl. Mater. Interfaces*, 2024, **16**, 26491–26499.

11 S. Haffouz, P. J. Poole, J. Jin, X. Wu, L. Ginet, K. Mnaymneh, D. Dalacu and R. L. Williams, *Appl. Phys. Lett.*, 2020, **117**, 113102.

12 E. D. Leshchenko and V. G. Dubrovskii, *Nanomaterials*, 2023, **13**, 1659.

13 M. Ghasemi, E. D. Leshchenko and J. Johansson, *Nanotechnology*, 2021, **32**, 072001.

14 K. A. Dick, C. Thelander, L. Samuelson and P. Caroff, *Nano Lett.*, 2010, **10**(9), 3494–3499.

15 M. E. Reimer, G. Bulgarini, A. Fognini, R. W. Heeres, B. J. Witek, M. A. M. Versteegh, A. Rubino, T. Braun, M. Kamp, S. Höfling, D. Dalacu, J. Lapointe, P. J. Poole and V. Zwiller, *Phys. Rev. B*, 2016, **93**, 195316.

16 D. Dalacu, K. Mnaymneh, J. Lapointe, X. Wu, P. J. Poole, G. Bulgarini, V. Zwiller and M. E. Reimer, *Nano Lett.*, 2012, **12**(11), 5919–5923.

17 T. Chiaramonte, L. H. G. Tizei, D. Ugarte and M. A. Cotta, *Nano Lett.*, 2011, **11**(5), 1934–1940.

18 J. Johansson, K. A. Dick, P. Caroff, M. E. Messing, J. Bolinsson, K. Deppert and L. Samuelson, *J. Phys. Chem. C*, 2010, **114**(9), 3837–3842.

19 F. Wang, C. Wang, Y. Wang, M. Zhang, Z. Han, S. Yip, L. Shen, N. Han, E. Y. B. Pun and J. C. Ho, *Sci. Rep.*, 2016, **6**, 32910.

20 S. Lehmann, J. Wallentin, D. Jacobsson, K. Deppert and K. A. Dick, *Nano Lett.*, 2013, **13**(9), 4099–4105.

21 S. Paiman, Q. Gao, H. H. Tan, C. Jagadish, X. Zhang and J. Zou, *J. Cryst. Growth*, 2013, **383**, 100–105.

22 P. J. Poole, D. Dalacu, X. Wu, J. Lapointe and K. Mnaymneh, *Nanotechnology*, 2012, **23**, 385205.

23 V. Zannier, F. Rossi, V. G. Dubrovskii, D. Ercolani, S. Battiato and L. Sorba, *Nano Lett.*, 2018, **18**(1), 167–174.

24 V. G. Dubrovskii, *Nucleation theory and growth of nanostructures*, Springer, Heidelberg – New York – Dordrecht – London, 2014.

25 V. G. Dubrovskii, N. V. Sibirev, X. Zhang and R. A. Suris, *Cryst. Growth Des.*, 2010, **10**, 3949.

26 C. Y. Wen, J. Tersoff, K. Hillerich, M. C. Reuter, J. H. Park, S. Kodambaka, E. A. Stach and F. M. Ross, *Phys. Rev. Lett.*, 2011, **107**, 025503.

27 D. Jacobsson, F. Panciera, J. Tersoff, M. C. Reuter, S. Lehmann, S. Hofmann, K. A. Dick and F. M. Ross, *Nature*, 2016, **531**, 317.

28 V. G. Dubrovskii, *Cryst. Growth Des.*, 2017, **17**, 2544.

29 V. G. Dubrovskii, N. V. Sibirev, N. N. Halder and D. Ritter, *J. Phys. Chem. C*, 2019, **123**, 18693.

30 F. Panciera, Z. Baraissov, G. Patriarche, V. G. Dubrovskii, F. Glas, L. Travers, U. Mirsaidov and J. C. Harmand, *Nano Lett.*, 2020, **20**, 1669.

31 V. G. Dubrovskii and F. Glas, *Cryst. Growth Des.*, 2024, **24**, 9660.

32 F. Glas, J. C. Harmand and G. Patriarche, *Phys. Rev. Lett.*, 2007, **99**, 146101.

33 T. Akiyama, K. Sano, K. Nakamura and T. Ito, *Jpn. J. Appl. Phys.*, 2006, **45**, L275.

34 M. Rosini and R. Magri, *ACS Nano*, 2010, **4**, 6021.

35 V. Pankoke, P. Kratzer and S. Sakong, *Phys. Rev. B: Condens. Matter Mater. Phys.*, 2011, **84**, 075455.

36 N. V. Sibirev, M. A. Timofeeva, A. D. Bolshakov, M. V. Nazarenko and V. G. Dubrovskii, *Phys. Solid State*, 2010, **52**, 1531.

37 K. A. Dick, P. Caroff, J. Bolinsson, M. E. Messing, J. Johansson, K. Deppert, L. R. Wallenberg and L. Samuelson, *Semicond. Sci. Technol.*, 2010, **25**, 024009.